Archive of Applied Mechanics 64 (1994) 206–222

Archive of
Applied Mechanics

Detection and simulation of small transverse cracks in rotating shafts

B. O. Dirr, K. Popp and **W. Rothkegel,** Hannover

Summary: The detection of small transverse cracks in rotating shafts is difficult. An advanced vibration monitoring method is proved in laboratory tests. It bases on an angle dependent sampling of the vibrational data and the comparison with a reference signal of the undamaged rotor. A finite crack element is developed from a spatial finite element analysis and is used for numerical simulations of the dynamic behaviour of cracked rotors. The results of the numerical simulations are compared with experimental data.

Zur Erkennung und Simulation kleiner, ebener Querrisse in Rotoren

Übersicht: Die Erkennung kleiner, ebener Querrisse in Rotoren ist schwierig. Ein erweitertes Verfahren zur Schwingungsüberwachung wird in Laborversuchen erprobt. Es basiert auf einer winkelgebergesteuerten Aufnahme der Rotorschwingungssignale und der Differenzbildung mit einem Referenzsignal des ungerissenen Rotors. Ein finites Rißelement wird aus räumlichen Finite-Elemente-Berechnungen entwickelt und zur numerischen Simulation des dynamischen Verhaltens angerissener Rotoren verwandt. Die Simulationsergebnisse werden mit den Meßergebnissen verglichen.

1 Introduction

Large turborotors are equipped with vibration monitoring systems to get informations about the vibrational state of a rotor and to detect possible defects. Some of these defects may be the change of the unbalance of the rotor or misalignment due to bad adjusted bearings or couplings. Very severe damage may occur due to a propagating transverse crack in a rotating shaft if it remains undetected. Some cases of damage due to cracked rotors and experiences using vibration monitoring techniques are reported in [1], [2], [4], [5], [8], [9], [10]. The problem with interpreting rotor vibrations is the seperation of some patterns in the vibration signal and its relations to certain defects. On the other hand the amplitudes caused by a crack remain small as long as the crack remains small. Therefore, only cracks of a depth of 20% or higher related to the shaft diameter can be detected with certainty by the commonly used vibration monitoring techniques.

An advanced vibration monitoring method is proved in laboratory tests for the detection of rotor cracks at a very early stage. The method makes use of an angle dependent sampling and averaging of the vibrational data and the comparison with a reference signal of the undamaged rotor. The experimental investigations are supported by theoretical examinations to get deeper insight in the influence of small cracks on the vibrational behaviour of rotors. For this purpose a finite crack element is developed from a three dimensional finite element analysis of the cracked rotor region. The results of the numerical simulations are compared with experimental data.

2 Advanced vibration monitoring technique

Prior to the description of the advanced vibration monitoring technique used in laboratory tests for crack detection the commonly applied vibration monitoring method is explained (see Fig. 1, left hand side): The shaft vibrations $s(t)$ are picked up by vibration transducers. In a practical case this is only

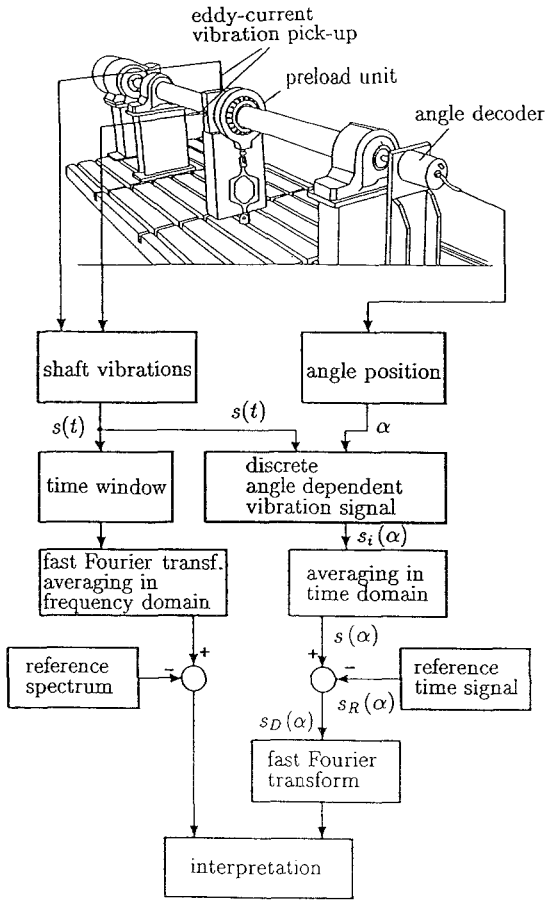

Fig. 1. Comparison between the commonly used vibration monitoring method (left-hand side) and the method of Imam (right-hand side)

possible close to the bearings. The vibration signals are weighted with an appropriate time window. The fast Fourier transformation of the vibration signal is calculated and the results are averaged in frequency domain. The spectrum is compared with a reference spectrum of the undamaged rotor. If there are some significant changes one looks for possible defects. The disadvantage of the described method with respect to crack detection is the fact that an increase of the second and higher harmonics, which are the indicators for a crack, is generally very small as long as a crack remains small.

2.1 The method of Imam

The applied advanced vibration monitoring technique bases on an US-patent hold by Imam [6]. Using this technique, Imam et al. [7] claim to detect cracks of a depth of 1%–2% of the rotor diameter in laboratory tests of rotating shafts. A comparison of his method with the commonly used vibration monitoring is shown in Fig. 1. To apply the method one needs an additional angle decoder to pick-up the vibration signals at discrete angle positions α. The time signal $s(t)$ becomes a discrete angle dependent signal $s_i(\alpha)$ where the subscript i denotes successive revolutions of the rotor. These angle dependent vibration signals are averaged over some hundreds of revolutions. Thus, one obtains an enhanced signal $s(\alpha)$ with reduced noise components and amplified repetitive components:

$$s(\alpha) = \frac{1}{M} \sum_{i=1}^{M} s_i(\alpha). \tag{1}$$

The enhanced signal $s(\alpha)$ is compared with an enhanced signal of the undamaged rotor $s_R(\alpha)$ called reference signal. The comparison is done by calculating the difference signal $s_D(\alpha)$ between the enhanced signal $s(\alpha)$ and the enhanced reference signal $s_R(\alpha)$:

$$s_D(\alpha) = s(\alpha) - s_R(\alpha). \tag{2}$$

This means that all stationary components in the difference signal are eliminated. The difference signal now contains mainly changes of the vibrational behaviour of the rotor. Then, the fast Fourier transform of the difference signal is calculated. An increase of the second and higher harmonics, called difference harmonics, indicates an incipient crack which can be detected at an earlier stage than by conventional vibration monitoring methods.

2.2 *Testing equipment and laboratory tests*

Fig. 2 shows a photograph of the testing device. The rotor in its two roller bearings is driven by a motor at constant speed. To simulate the weight of real turborotors the rotor is preloaded by a loading unit. This leads to a three-point-bending of the shaft. To get a crack at a known axial position of the rotor a small initial cut is made near the load acting plane. The cut should be as small as possible because it is intended to detect a crack at a very early stage. On the other hand the cut has to be deep enough to initiate the crack at the desired position. Some problems of the crack initiation by

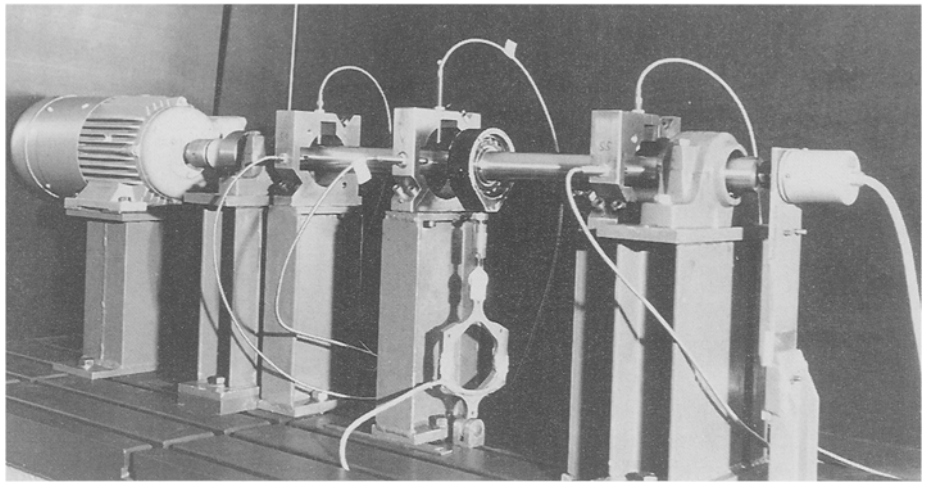

Fig. 2. Photograph of the testing equipment

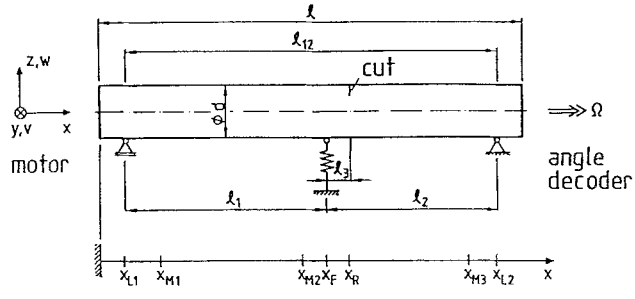

	Z..	V..		Z..	V..	
$d\,[mm]$	20	40	$d\,[mm]$	20	40	
$\ell\,[mm]$	490	900	$x_{L1}\,[mm]$	80	100	bearing plane 1
$\ell_{12}\,[mm]$	370	740	$x_{L2}\,[mm]$	450	840	bearing plane 2
$\ell_1\,[mm]$	203	405	$x_{M1}\,[mm]$	219.5	190	measurement plane 1
$\ell_2\,[mm]$	167	335	$x_{M2}\,[mm]$	344.5	430	measurement plane 2
$\ell_3\,[mm]$	17	35	$x_{M3}\,[mm]$	-	750	measurement plane 3
			$x_F\,[mm]$	283	505	load acting plane
			$x_R\,[mm]$	300	540	plane of the cut

$\frac{\ell_{12}}{d} = 18.5\,,\quad \frac{\ell_1 + \ell_3}{d} = 11\,,\quad \frac{\ell_1}{\ell_2} = 1.2\,,\quad \frac{\ell}{d} = 10.1$

Fig. 3. Dimensions of the testing equipment

cut will be discussed later in detail. Opposite to the motor the angle decoder is adjusted at the rotor. The vibration signals can be picked up in horizontal and vertical direction by eddy-current vibration pick-ups. The number of measurement planes are dependent on the rotor length. Fig. 3 shows the dimensions of the two rotor types used together with the location of the measurement planes, the load acting plane and other parameters of the laboratory tests.

The signal processing is shown in Fig. 4. The measurements in the different planes are sampled by a scanner which is controlled by a process computer. The vibration signals pass an analog low-frequency preamplifier and then a digital adjustable amplifier which is adjusted by the process computer before every measurement cycle is started. Now the vibration signal is fed to an analog-to-digital converter which is read out from the process computer at discrete angle positions prescribed by the angle decoder. The process computer averages the signals angle dependent over some hundreds of revolutions, calculates the difference signal and performs the fast Fourier transformation to assess the rotor state.

2.3 Experimental results

Two different types of test rotors are used (see Fig. 3). One type has a diameter of 20 mm (called Z..-rotor) and a length of 490 mm, the other one has a diameter of 40 mm (called V..-rotor) and a length of 900 mm. Fig. 5a) shows a photograph of one of the fractured cross-sections of the V22-rotor (diameter d = 40 mm). Here, dark lines called beach marks are visible. A beach mark is set by removing the load and driving the rotor for about 100000 revolutions. The beachs marks are very important for evaluating the experiments because they give the true relation between the vibration signals and the depth and the form of the crack front. In Fig. 5b) the beach marks drawn from the photograph of the cracked area are outlined and the definition of the crack depth is given.

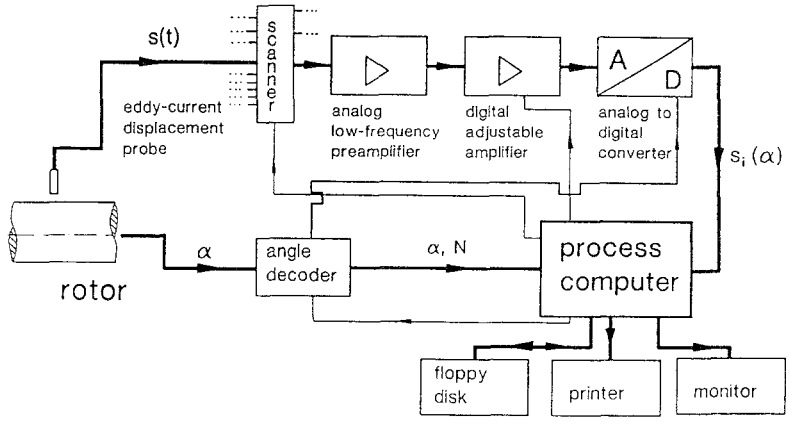

Fig. 4. Block diagram of the measurement devices

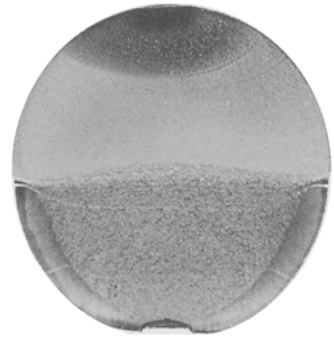

a

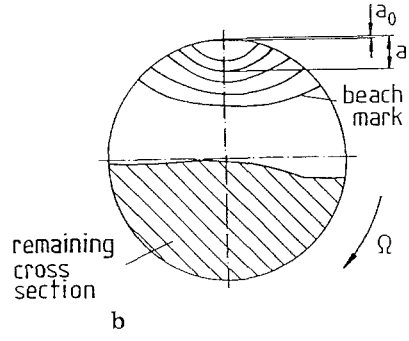

b

5

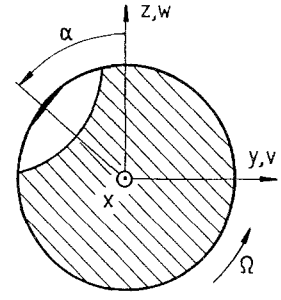

6

Fig. 5 and **6. 5a** Photograph of the fractured cross-section of the V22-rotor. **b** Beach marks, drawn from the photograph of the cracked area; **6** Definition of the angle α

The experimental experience shows that it is difficult to manufacture a sufficiently small cut for starting the cracking process accurately at the desired location. Two methods producing cuts have been tested: an electroerosive technique with a wire of only 0.1 mm of diameter and a metal cutting technique using a very pointed cutting tool. The investigations make clear that the electroerosive technique is more suited for the crack initiation than the metal cutting technique if the depth of the cut is 0.2 mm or deeper. In cases of very small cuts it turned out that the mounting of the preload bearing caused much deeper initial defects, and thus, lead to cracking of one half of the shafts in the load acting plane and not, as desired, from the initial cut. In this paper only results are presented for test rotors with a crack starting from the initial cut. But the differences in the vibrational behaviour to rotors where the crack started in the load acting plane are only small because of the nearby located axial crack positions.

In the following results of some of the investigted 18 test rotors are presented. More detailed results are reported in [11] and [12]. For the discussion purpose the definition of angle α between the spaced fixed x, y, z-coordinate system and the crack-area centerline is given in Fig. 6. The amplitudes of the vibration signals in the vertical z-direction are much smaller than the amplitudes of the

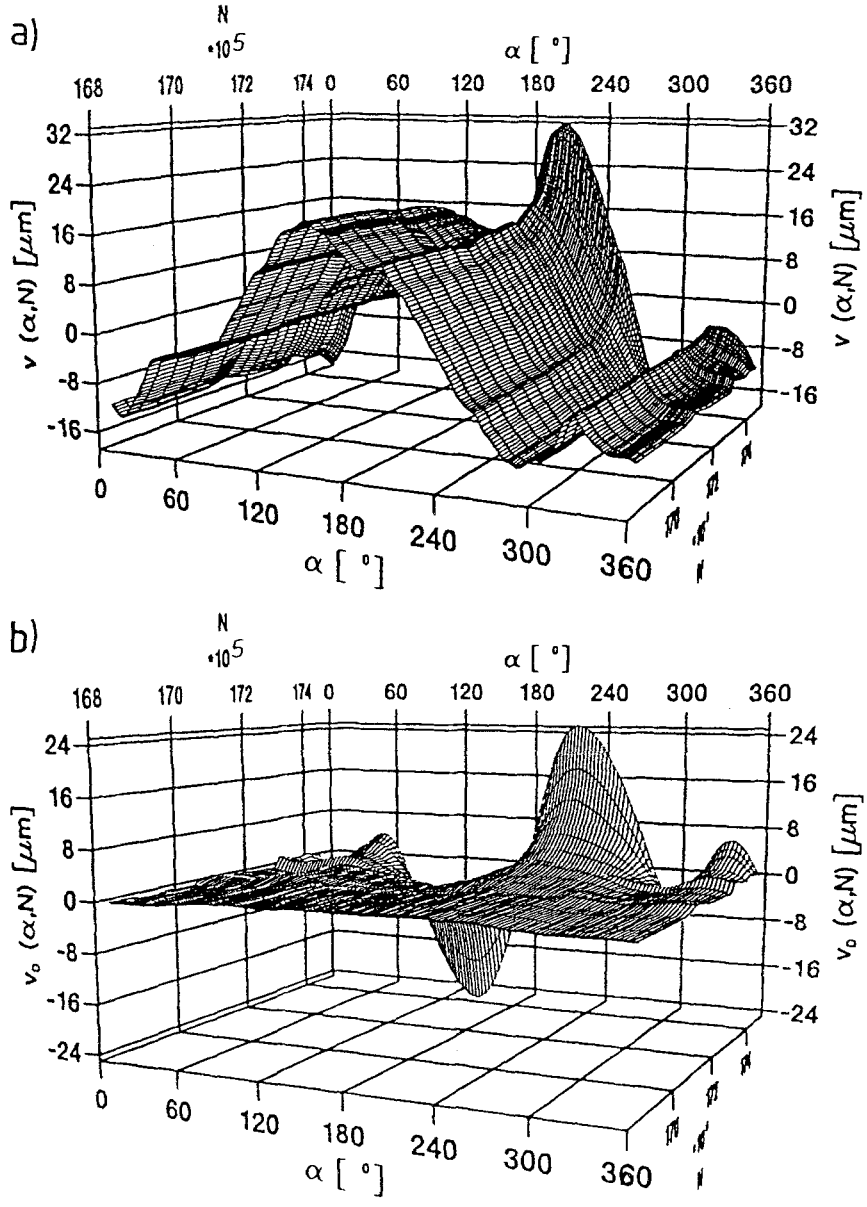

Fig. 7. **a** Averaged horizontal vibration signal $v(a/d, \alpha)$, V23-rotor: plane 2, $n = 1560$ rpm, $F_{V0} = -7500$ N. **b** Averaged horizontal difference signal $v_D(a/d, \alpha)$, V23-rotor: plane 2, $n = 1560$ rpm, $F_{V0} = -7500$ N, $N_{Ref} = 16{,}500{,}000$

vibration signals in the horizontal y-direction because of the vertical preloading of the rotor. Therefore the signals in horizontal direction are much more suited for the crack detection in the laboratory tests and here only these results are presented.

In Fig. 7 a) results for the horizontal vibration signal of the V23-rotor in the measurement plane 2 near the load acting plane (see Fig. 3) are presented. The signal $v(\alpha, N)$ is plotted against the angle α and the number N of revolutions. The number of revolutions starts at $N = 16.8$ millions, that means about 500,000 revolutions before the first beach mark was set at a crack depth of $a/d = 5\%$ and goes up to the third beach mark with a crack depth of $a/d = 17.5\%$ at $N = 17.45$ millions. Every line parallel to the α–v-plane represents one signal averaged over 500 successive revolutions. Lines parallel to the N–v-plane indicate angle positions where the vibration signals were picked up (256 samplings/revolution). There are only slight changes of the vibration signals at the end of the plotted range of revolutions.

Fig. 7 b) shows the trend of the difference signal $v_D(\alpha, N)$ in the same range of revolutions, calculated with an enhanced reference signal picked up at $N = 16.5$ millions of revolutions. Here, a significant increase of the amplitudes of the difference signal starts at about $N = 17.1$ millions of revolutions. From the difference signal v_D the crack growing can be seen much clearer than from the absolute signal v and therefore the advantage of the method of Imam is obvious in this case.

Fig. 8 a) shows the first three harmonics $\hat{v}_{k\Omega}$ of the horizontal vibration signal v, plotted in Fig. 7 a), and Fig. 8 b) the first three harmonics of the horizontal difference signal $\hat{v}_{Dk\Omega}$ (called difference harmonics), plotted in Fig. 7 b), in the same range of revolutions. Here, a slight decrease of the first and second harmonic of the absolute signal can be seen up to the second beach mark wehre the crack depth is about $a/d = 13.75\%$. In contrast to this all three difference harmonics show a clear monotonous increase starting at about $N = 17.1$ millions of revolutions. The second difference harmonic indicates at first the existence of a crack.

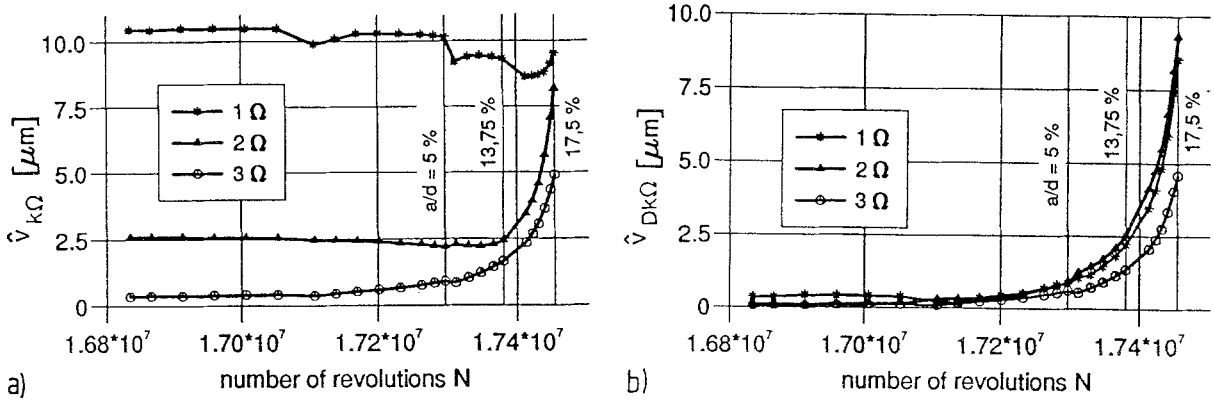

Fig. 8. **a** Amplitudes of the first three harmonics of the horizontal vibration signal, V23-rotor: plane 2, $n = 1560$ rpm, $F_{V0} = -7500$ N. **b** Amplitudes of the first three harmonics of the horizontal difference signal, V23-rotor: plane 2, $n = 1560$ rpm, $F_{V0} = -7500$ N, $N_{Ref} = 16{,}500{,}000$

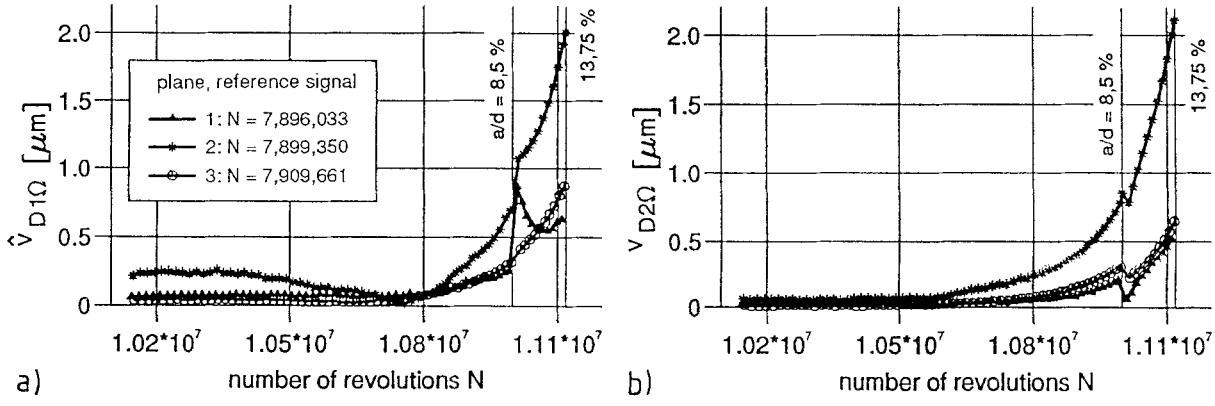

Fig. 9. **a** First difference harmonics $\hat{v}_{D1\Omega}$ of the V22-rotor (planes 1–3, $n = 1560$ rpm, $F_{V0} = -6500$ N, $N_{Ref} = 7{,}900{,}000$). **b** Second difference harmonics $\hat{v}_{D2\Omega}$ of the V22-rotor (planes 1–3, $n = 1560$ rpm, $F_{V0} = -6500$ N, $N_{Ref} = 7{,}900{,}000$)

In Fig. 9 the influence of the three measurement planes on the crack detection by vibration monitoring is visualized by means of the V22-rotor. The first and second difference harmonics of all three measurement planes are plotted against the number of revolutions. The range of revolutions N starts about 800,000 revolutions before the first beach mark was set and comprises the second beach mark with a related crack depth of $a/d = 13.75\%$. It can be seen that the amplitudes in the second measurement plane, that is near the preload unit and near the crack location, are higher than in the outer measurement planes 1 and 3. But also the increase of the amplitudes with growing crack in the outer measurement planes is sufficient for crack detection.

In Fig. 10 the influence of the rotor speed n is documented. In the diagram to the left results for the V24-rotor driven at a speed of $n = 1560$ rpm and in the right hand diagram those for the V25-rotor driven at a speed of $n = 3060$ rpm are plotted against the crack depth a/d. The first three difference harmonics $\hat{v}_{Dk\Omega}$ of the horizontal vibration signal in the measurement plane 2 are shown. It can be seen, that the increase of the second difference harmonic $\hat{v}_{D2\Omega}$ for similar crack depths is more significant at higher rotor speed.

In Fig. 11 results of one of the test rotors with a diameter of 20 mm are considered. Again the harmonics of the absolute signal (left hand diagram) and the difference signal (right hand diagram) are compared. Now the first three harmonics $\hat{v}_{k\Omega}$ and difference harmonics $\hat{v}_{Dk\Omega}$ of the horizontal vibration signal in the measurement plane 1 of the Z07-rotor are plotted against the related number N/N_{max} of revolutions, where N_{max} is the maximum number of revolutions of this test rotor. The ordinates are logarithmically scaled. An auxiliary axis marks the crack depths at certain numbers of revolutions, where beach marks have been set in the fractured structure. It can be seen that the first harmonic $\hat{v}_{1\Omega}$ of

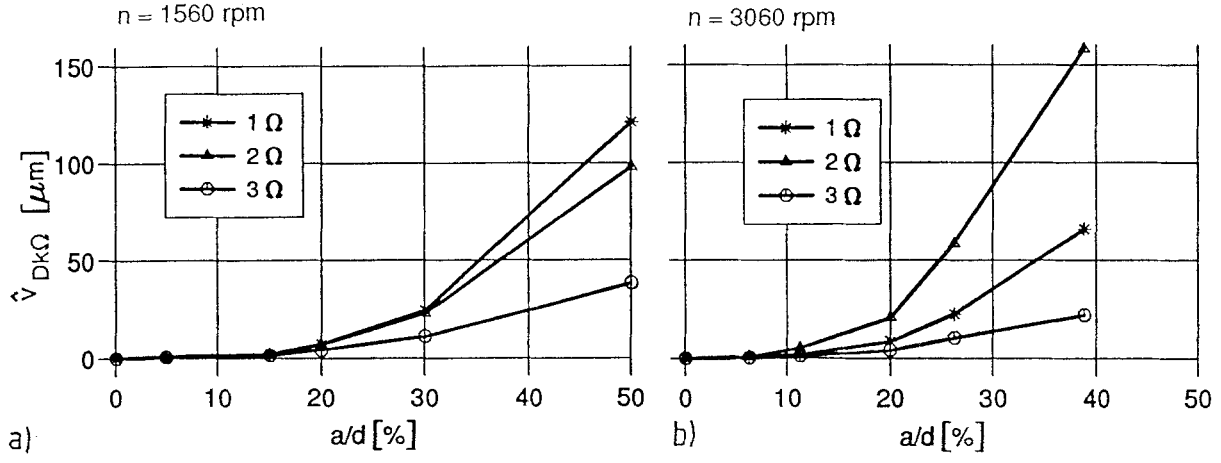

Fig. 10. **a** Difference harmonics of the V24-rotor (plane 2, $n = 1560$ rpm, $F_{V0} = -7500$ N, $N_{Ref} = 333{,}916$). **b** Difference harmonics of the V25-rotor (plane 2, $n = 3060$ rpm, $F_{V0} = -7500$ N, $N_{Ref} = 937{,}244$)

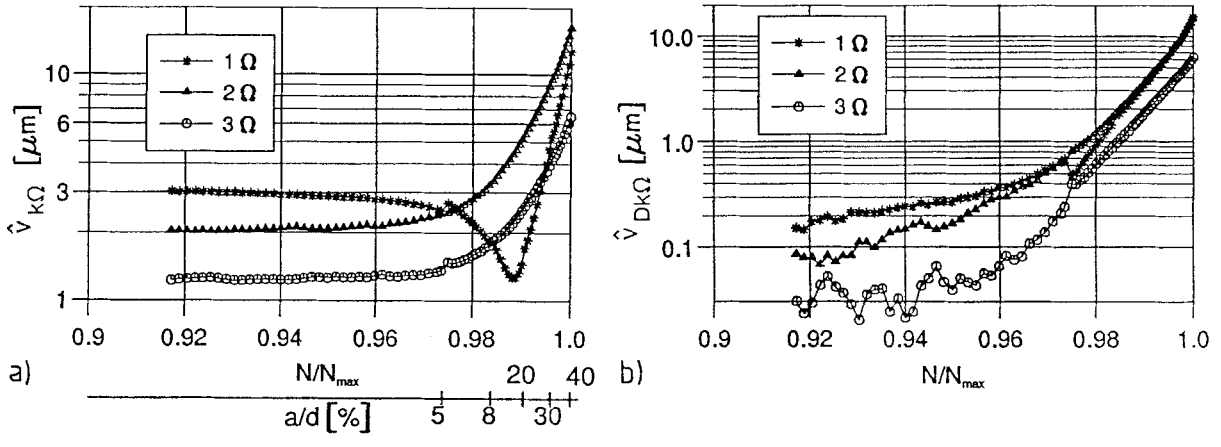

Fig. 11. **a** Harmonics of the Z07-rotor (plane 1, $n = 1560$ rpm, $F_{V0} = -2000$ N, $N_{max} = 9{,}539{,}414$). **b** Difference harmonics of the Z07-rotor (plane 1, $n = 1560$ rpm, $F_{V0} = -2000$ N, $N_{max} = 9{,}539{,}414$, $N_{Ref} = 8{,}157{,}434$)

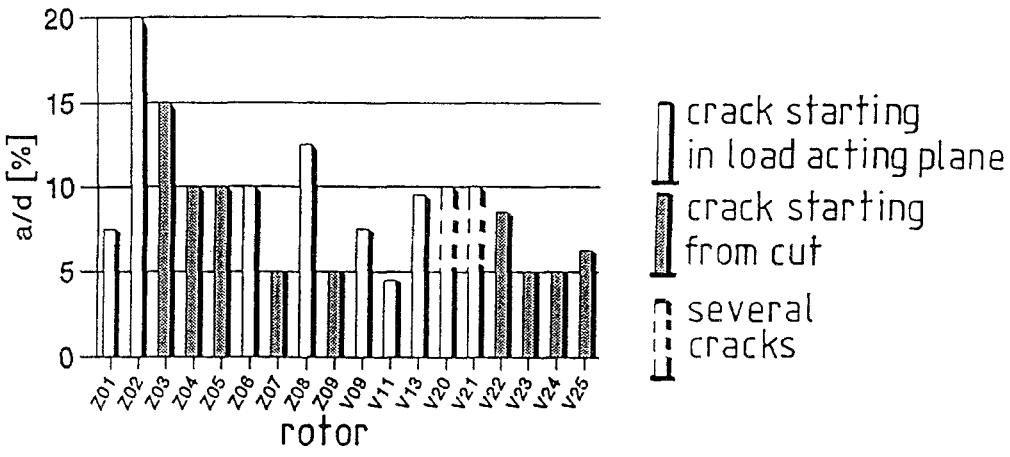

Fig. 12. Crack depths at the first beach mark of all investigated experimental rotors

the absolute signal decreases up to a crack depth of $a/d = 20\%$. The three difference harmonics $\hat{v}_{Dk\Omega}$ show all a monotonous increase for $N/N_{\max} \geqq 0.96$. The second difference harmonic $\hat{v}_{D2\Omega}$ indicates at first the existance of a crack. In comparison with all other investigated test rotors it can be seen that there are only slightly differences in he vibrational behaviour of rotors with a diameter of 20 mm and 40 mm.

In Fig. 12 the crack depths related to the first beach mark of all investigated test rotors are given. The test rotors V20 and V21 had several cracks at different locations so that no clear relation between the first beach mark and the crack depth can be given. It can be seen that it is possible to detect cracks of a depth of $a/d = 5\%$ with the advanced vibration monitoring technique.

3 Numerical simulations

The aim of the theoretical investigations is to develop a finite crack element for numerical simulations of the dynamic behaviour of cracked rotors. On this base the sensitivity of the rotor vibrations with respect to cracks can be studied numerically.

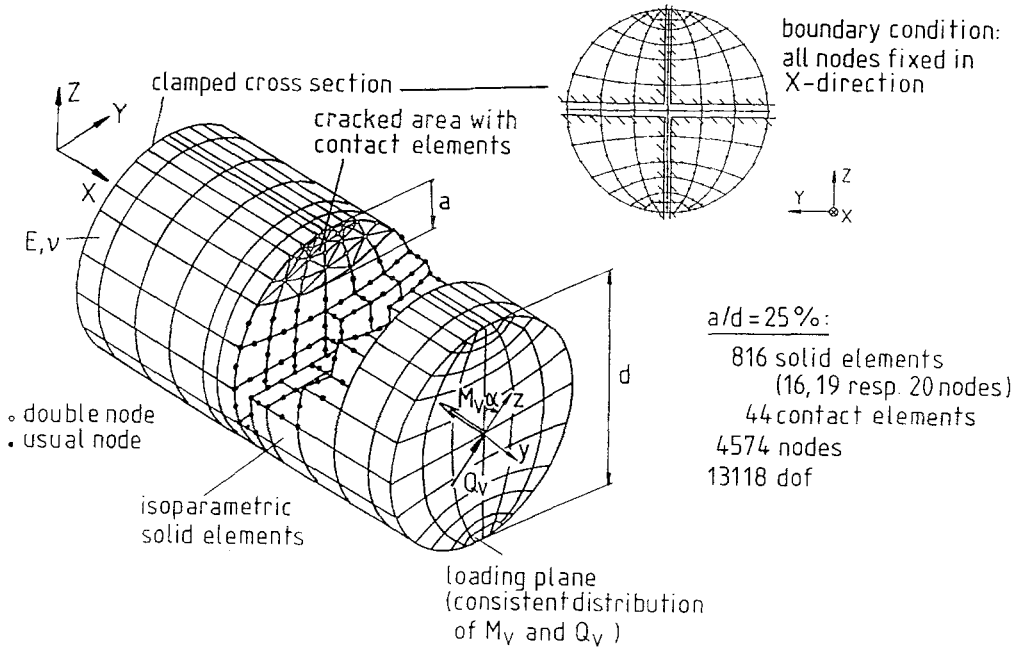

Fig. 13. Spatial finite element model of the cracked rotor section ($d = 40$ mm, $\ell = 70$ mm, $\ell_R = 35$ mm, $E = 200{,}000\ N/\text{mm}^2$, $\nu = 0.3$, $M_V = 725$ Nm, $Q_V = 2737\ N$)

3.1 *Spatial finite element analysis of a cracked rotor section*

Fig. 13 shows a spatial finite element model of the cracked rotor region of one of the test rotors with a diameter of 40 mm. It consists of more than 800 isoparametric solid elements with 20, 19 and 16 nodes, respectively. The whole model has more than 4500 nodes and more than 13000 degrees of freedom. The cracked area is modelled using a double node technique and special contact elements [3]. The used contact elements allow the consideration of friction between the cracked areas. In our model no friction has been regarded. The model is shown in Fig. 13 for a crack depth of $a/d = 25\%$. The consistent loading distribution corresponds to the static loading conditions of the experimental rotor. Here, one end of the spatial finite element model is clamped and the loading rotates instead of the stationary loading and the rotation of the shaft in the experiment.

In Fig. 14 the pressure distribution on the contact elements for a crack depth of $a/d = 25\%$ is shown. From $\alpha = 0°$ to $\alpha = 45°$ the crack is fully closed. Then it begins to open and it is fully open for $120° \leqq \alpha \leqq 240°$. This crack opening and closing behaviour is called the breathing of a crack and is symmetric to the angle $\alpha = 180°$.

In Fig. 15 the displacements v and w of the node B in y-direction and z-direction, respectively, are plotted against the angle α ($\Delta\alpha = 15°$) and the related crack depths a/d ($a/d = 0\%, 5\%, 10\%, 17.5\%, 25\%$). The node B is the node in the middle of the loading plane. For small crack depths the changes of the displacements as a function of the angle α are very small.

3.2 *Development of a finite crack element of beam type*

The spatial finite element model with more than 13000 degrees of freedom exceeds tolerable computing amount when it is used for the calculation of the dynamic behaviour of the cracked experimental rotor. Therefore, the results of the three-dimensional calculations are condensed to a finite crack element of beam type. This crack element should represent approximately the stiffness behaviour of the spatial finite element model. The procedure is similar to the one reported by Schmalhorst in [13]. The beam type element is described by two nodes A and B (see Fig. 16) with eight degrees of freedom. The 8×8-stiffness matrix $\mathbf{K}_R(a/d, \alpha)$ of the crack element reads:

$$\begin{bmatrix} k_{11} & k_{12} & k_{13} & k_{14} & k_{15} & k_{16} & k_{17} & k_{18} \\ k_{21} & \dots & \dots & \dots & \dots & \dots & \dots & k_{28} \\ \dots & & & & & & & \\ \dots & & & & & & & \\ \dots & & & & & & & \\ \dots & & & & & & & \\ \dots & & & & & & & \\ k_{81} & k_{82} & k_{83} & k_{84} & k_{85} & k_{86} & k_{87} & k_{88} \end{bmatrix} \begin{bmatrix} v_A \\ w_A \\ \varphi_{yA} \\ \varphi_{zA} \\ v_B \\ w_B \\ \varphi_{yB} \\ \varphi_{zB} \end{bmatrix} = \begin{bmatrix} Q_{yA} \\ Q_{zA} \\ M_{yA} \\ M_{zA} \\ Q_{yB} \\ Q_{zB} \\ M_{yB} \\ M_{zB} \end{bmatrix}. \tag{3}$$

The above symmetric matrix is assembled of ten independent coefficients $A(a/d, \alpha)$ to $K(a/d, \alpha)$:

$$\mathbf{K}_R(a/d, \alpha) = \begin{bmatrix} A & G & H & B & -A & -G & -G\ell - H & A\ell - B \\ & D & -E & I & -G & -D & -D\ell + E & G\ell - I \\ & & F & K & -H & E & E\ell - F & H\ell - K \\ & & & C & -B & -I & -I\ell - K & B\ell - C \\ & & & & A & G & G\ell + H & -A\ell + B \\ \text{symmetric} & & & & & D & D\ell - E & -G\ell + I \\ & & & & & & D\ell^2 - 2E\ell + F & -G\ell^2 + (I - H)\ell + K \\ & & & & & & & A\ell^2 - 2B\ell + C \end{bmatrix} \tag{4}$$

where ℓ is the length of the crack element.

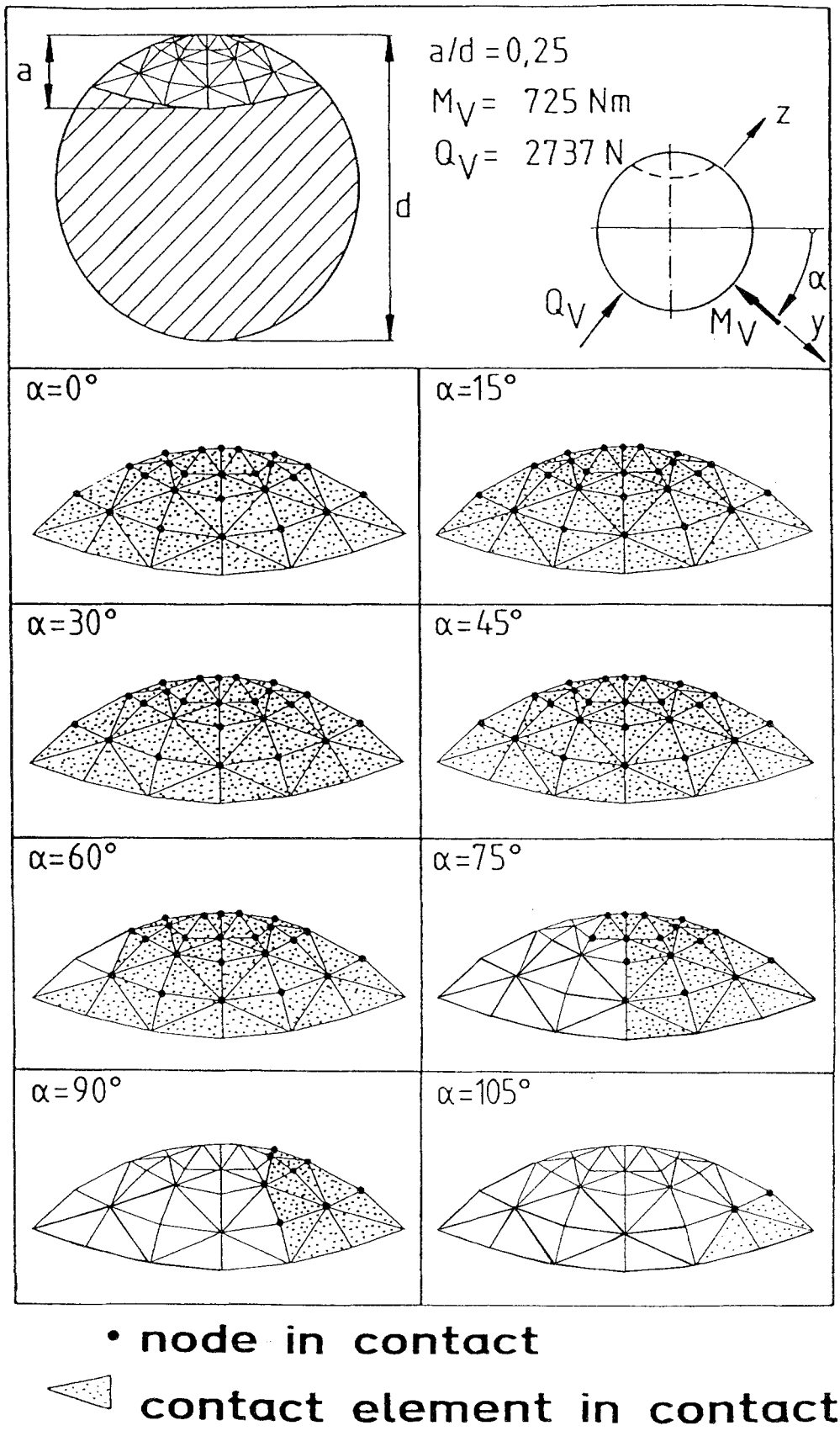

Fig. 14. Contact pressure distribution

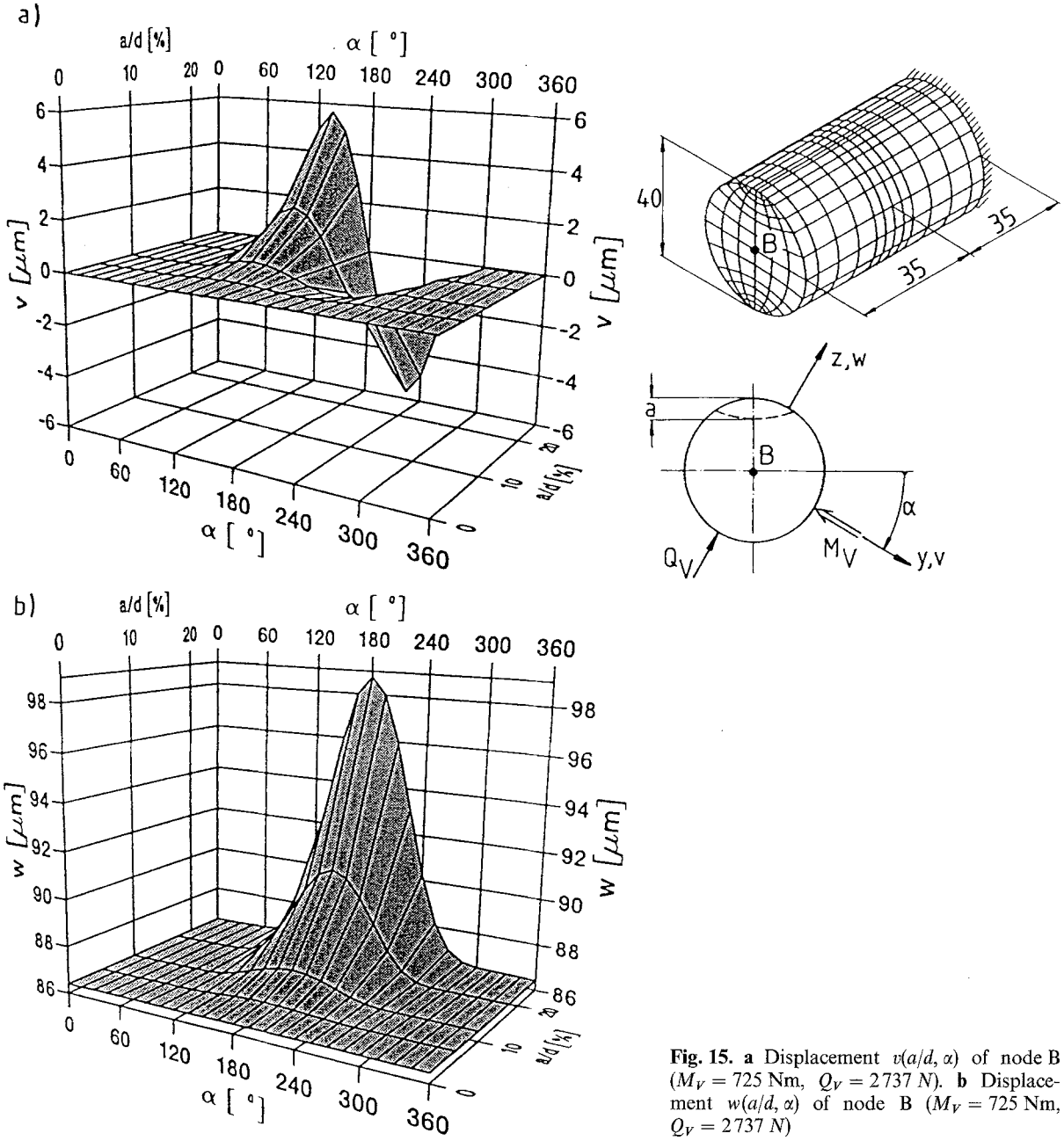

Fig. 15. **a** Displacement $v(a/d, \alpha)$ of node B ($M_V = 725$ Nm, $Q_V = 2737$ N). **b** Displacement $w(a/d, \alpha)$ of node B ($M_V = 725$ Nm, $Q_V = 2737$ N)

This stiffness matrix fulfills the force and moment equilibrium of the crack element. Rigid body motions and rotations are possible with respect to the y- and z-axis. The coefficients A to C represent the bending in the x–y-plane, the coefficients D to E the bending in the x–z-plane and the coefficients F to K couple the two bending planes.

The coefficients A to K are calculated for certain crack depths a/d and angle positions α using the load and deflection states of the nodes A and B of the spatial finite element model (see Fig. 16). For the set $i = I$ of loading one gets the following load vector $\mathbf{f}^I$ and the deflection vector $\mathbf{d}^I$:

$$\mathbf{f}^I = [Q_{yA}^I Q_{zA}^I M_{yA}^I M_{zA}^I Q_{yB}^I Q_{zB}^I M_{yB}^I M_{zB}^I]^T, \tag{5}$$

$$\mathbf{d}^I = [v_A{}^I w_A{}^I \varphi_{yA}^I \varphi_{zA}^I v_B{}^I w_B{}^I \varphi_{yB}^I \varphi_{zB}^I]^T. \tag{6}$$

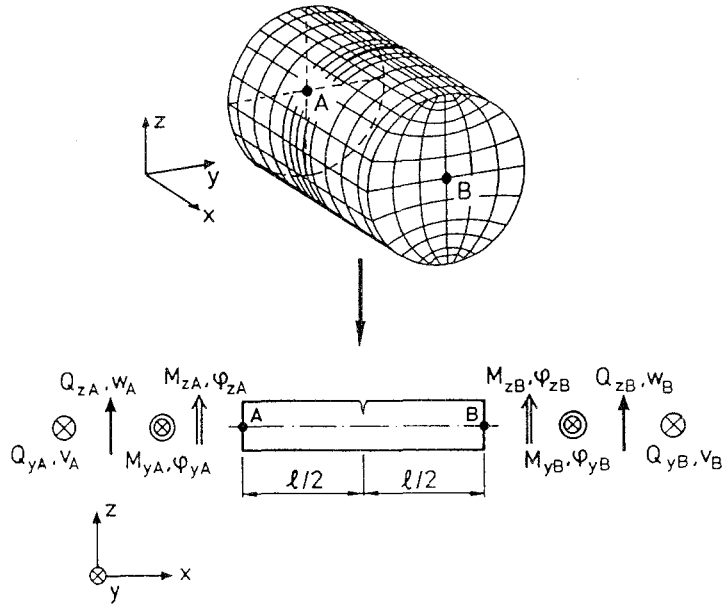

Fig. 16. Condensation of the 3-D-FE-model to a finite crack element of beam type

Using (5) and (6) one can describe the deflection state of the nodes A and B of the spatial finite element model:

$$a^I = \frac{v_B{}^I - v_A{}^I - \varphi_{zB}^I \ell}{\ell}, \tag{7}$$

$$b^I = \frac{w_B{}^I - w_A{}^I + \varphi_{yB}^I \ell}{\ell}, \tag{8}$$

$$c^I = \varphi_{zB}^I - \varphi_{zA}^I, \tag{9}$$

$$d^I = \varphi_{yB}^I - \varphi_{yA}^I, \tag{10}$$

where the abbreviations a^I to d^I have been introduced.

For every independent set of loading $i = I, II, III, \ldots$ one gets four equations for the calculation of the ten unknown coefficients A to K. With three or more independent sets of loading for one crack depth a/d and one angle α one gets an overdetermined set of equations:

$$\begin{bmatrix}
a^I & c^I & 0 & 0 & 0 & 0 & b^I & d^I & 0 & 0 \\
0 & 0 & 0 & b^I & -d^I & 0 & a^I & 0 & c^I & 0 \\
0 & 0 & 0 & b^I & -b^I - d^I & d^I & a^I & a^I & c^I & c^I \\
-a^I & a^I - c^I & c^I & 0 & 0 & 0 & -b^I & -d^I & b^I & d^I \\
a^{II} & c^{II} & 0 & 0 & 0 & 0 & b^{II} & d^{II} & 0 & 0 \\
\vdots & \vdots & \vdots & \vdots & \vdots & \vdots & \vdots & \vdots & \vdots & \vdots \\
\vdots & \vdots & \vdots & \vdots & \vdots & \vdots & \vdots & \vdots & \vdots & \vdots
\end{bmatrix}
\begin{bmatrix}
A\ell \\ B \\ C/\ell \\ D\ell \\ E \\ F/\ell \\ G\ell \\ H \\ I \\ K/\ell
\end{bmatrix}
=
\begin{bmatrix}
Q_{yB}^I \\ Q_{zB}^I \\ M_{yB}^I/\ell \\ M_{zB}^I/\ell \\ Q_{yB}^{II} \\ \vdots \\ \vdots
\end{bmatrix} \tag{11}$$

or

$$^{m}\mathbf{R}^{10}\,{}^{10}\mathbf{k} = {}^{m}\mathbf{b} \quad \text{with } m \geqq 12. \tag{12}$$

The least-squares solution of (11) leads to the coefficients A to K:

$$\mathbf{k} = (\mathbf{R}^T\mathbf{R})^{-1}\,\mathbf{R}^T\mathbf{b}. \tag{13}$$

For the selection of independent sets of loading to create the overdetermined equation (12) the following procedure is suitable (for further details see [12]). Every overdetermined equation is build up from eight independent sets of loading which describe the *same crack opening behaviour*. The sets of loading are superposed of the static loading condition of the experiment (see Fig. 13) of the *cracked* rotor and one of eight test loading conditions (see Fig. 17) of the *uncracked* rotor. The amount of the test loading condition is only 1% of the static loading of the experiment:

$$Q_{Ti} = \frac{1}{100}\,|Q_V|, \quad i = 1, 2, 3, 4, \tag{14}$$

$$M_{Ti} = \frac{1}{100}\,|M_V|, \quad i = 5, 6, 7, 8. \tag{15}$$

Thus, the static loading condition of the experiment dominates the crack opening behaviour for every set of loading. As a result the coefficient $G(a/d, \alpha)$ is plotted in Fig. 18 against the angle α and the related crack depth a/d.

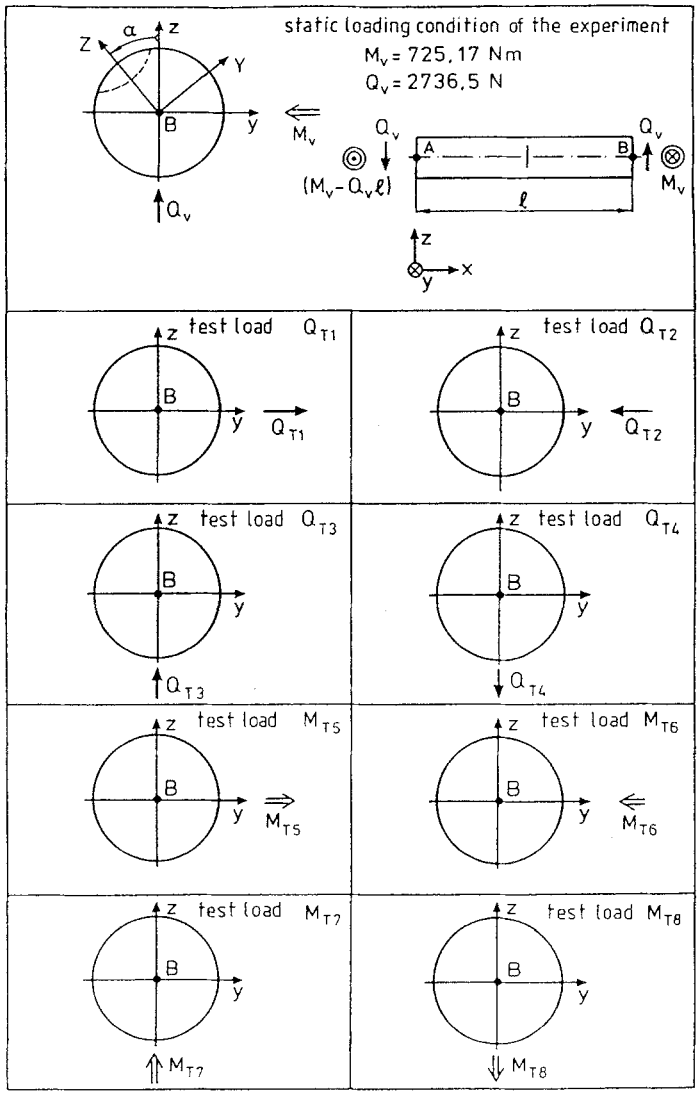

Fig. 17. Selection of sets of loading

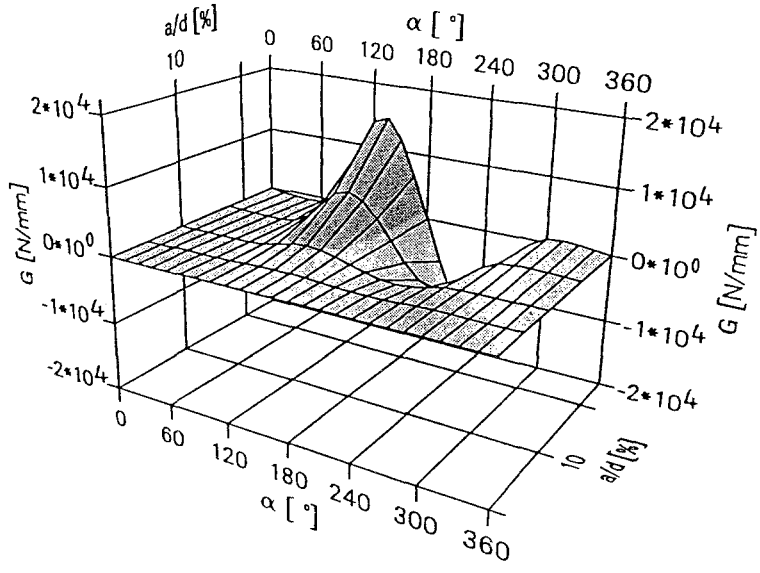

Fig. 18. Coefficient $G(a/d, \alpha)$ of the stiffness matrix of the crack element

$d_\ell = 0.1\,Ns/mm$, $d_h = 0.5\,Ns/mm$, $d_v = 3\,Ns/mm$, $k_\ell = 10^8\,N/mm$, $k_V = 17600\,N/mm$, $m_K = 1.2\,kg$, $m_V = 1.5\,kg$, $E = 200000\,N/mm^2$, $\rho = 7.85\,kg/dm^3$, $D_1 = D_2 = 2 \cdot 10^{-4}$

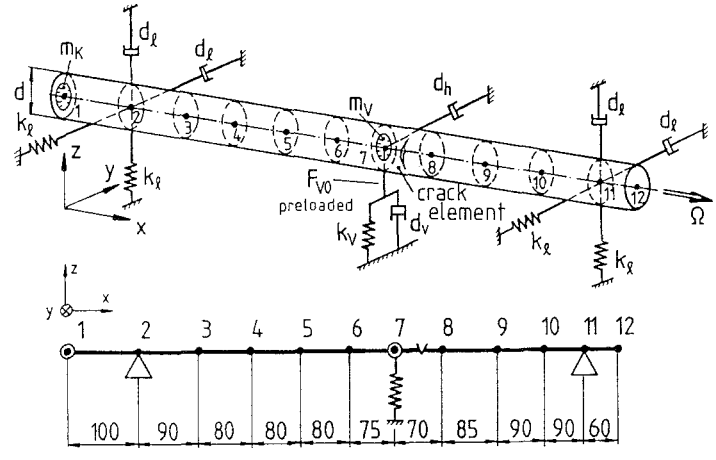

Fig. 19. Finite element model of the experimental rotor

3.3 Finite element model of the experimental rotor

The finite crack element is used together with normal beam elements (Euler-Bernoulli beam theory) to create a finite element model of the experimental rotor (see Fig. 19). The differential equation of the rotor reads:

$$\mathbf{M}\ddot{\mathbf{d}}(t) + (\mathbf{D}_\ell + \mathbf{D}_m)\,\dot{\mathbf{d}}(t) + \left(\mathbf{K}_\ell + \mathbf{K}(a/d, \alpha)\right)\mathbf{d}(t) = \mathbf{f}(a/d, \alpha) + \mathbf{f}_u(\Omega t) \tag{16}$$

with

$$\alpha = \mathrm{mod}\,(\Omega t, 2\pi) \tag{17}$$

and the initial conditions

$$\mathbf{d}(t = 0) = \mathbf{d}(\alpha = 0°) = \mathbf{h}(\alpha = 0°)\,F_{V0} \quad \text{and} \quad \dot{\mathbf{d}}(t = 0) = \mathbf{0}. \tag{18}$$

In (16) describes $\mathbf{M}$ the mass matrix, $\mathbf{D}_\ell$ the damping matrix of the discrete viscous dampers at the bearings, $\mathbf{D}_m$ a damping matrix regarding structural damping and $\mathbf{K}_\ell$ the stiffness matrix describing the stiffness of the bearings. The stiffness matrix $\mathbf{K}$ now contains the stiffness matrix of the crack

element $\mathbf{K}_R(a/d, \alpha)$. The vector $\mathbf{f}(a/d, \alpha)$ describes the preloading of the experimental rotor and can be calculated in a static analysis:

$$\mathbf{f}(a/d, \alpha) = \mathbf{h}(a/d, \alpha)\, F_V, \tag{19}$$

where $\mathbf{h}$ is the column of the compliance matrix of $\mathbf{K}$ which is related to the degree of freedom in z-direction of the loading device, and F_V is the force in the preloading device. By the vector $\mathbf{f}_u(\Omega t)$ unbalance forces can be considered.

The solution of equation (16) is done using a modal approach with a finite number of the lowest eigenmodes Φ_i ($i = 1, 2, \ldots, 12$) of the cracked, undamped system with open crack and a numerical integration of the resulting differential equation in state space representation using a Runge-Kutta-Merson method. For a comparison with experimental data the nodes 3, 6 and 10 (see Fig. 19) are used which represent the measurement planes 1, 2 and 3 of the experiment (see Fig. 3).

4 Comparison of simulation results with experimental data

In Fig. 20 the enhanced horizontal difference signal of the V22-rotor at a crack depth of $a/d = 8.5\%$ for the second and third measurement plane is plotted for one revolution of the rotor. In the same diagram the results of the numerical simulation at the corresponding nodes 6 and 10 are plotted. Good agreement between measurement and numerical simulation can be stated.

In Fig. 21 similar results for the V25-rotor are shown. This rotor was driven at $n = 3060$ rpm, which is nearly double the speed of the V22-rotor. For one revolution results for the second

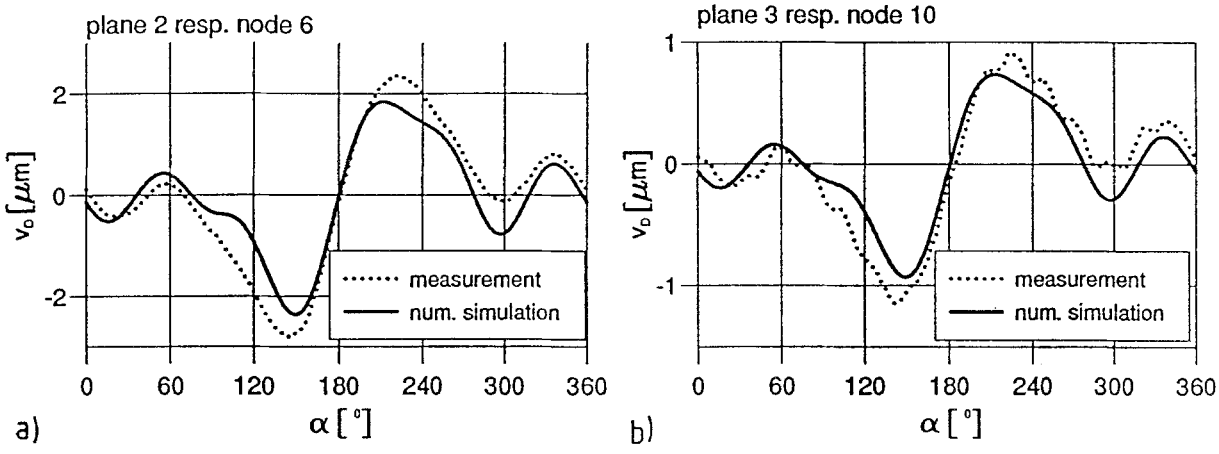

Fig. 20. Comparison between measurement and numerical simulation (V22-rotor, $n = 1560$ rpm, $F_{V0} = -6500\,N$, $a/d = 8.5\%$, $N_{Ref} = 10{,}150{,}000$): **a** plane 2 respective node 6, **b** plane 3 respective node 10

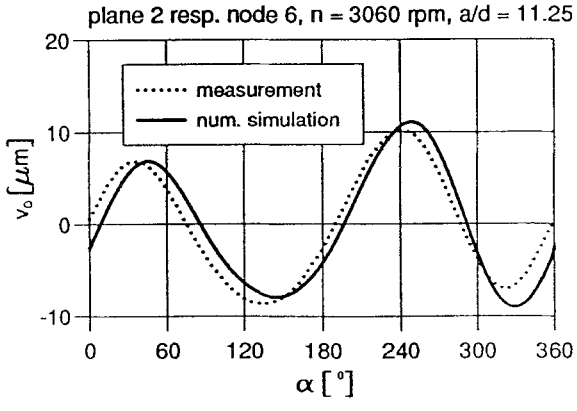

Fig. 21. Comparison between measurement and numerical simulation (V25-rotor, $n = 3060$ rpm, $F_{V0} = -7500\,N$, $a/d = 11.25\%$, $N_{Ref} = 950{,}000$, plane 2 respective node 6)

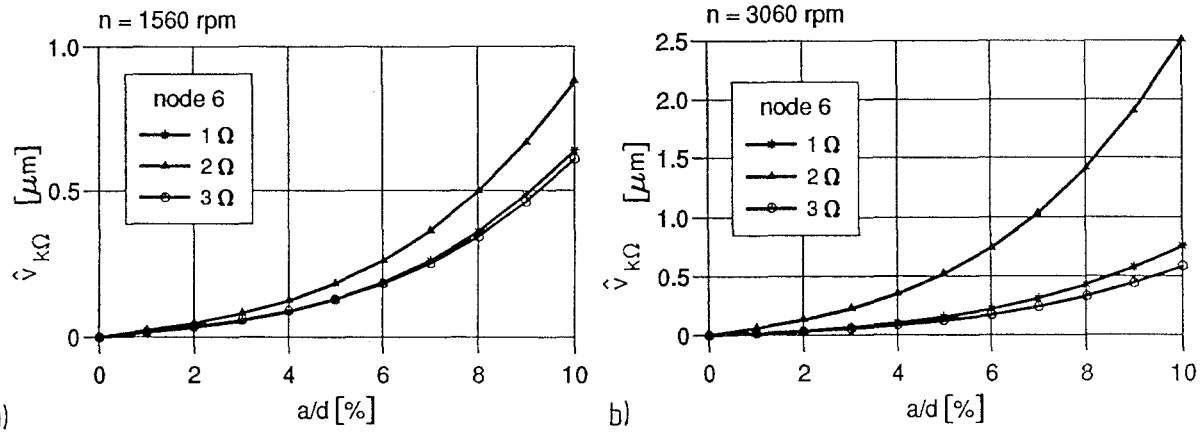

Fig. 22. Numerical simulation, horizontal vibration signal, $F_{V0} = -6500\ N$, node 6: **a** $n = 1560$ rpm, **b** $n = 3060$ rpm

measurement plane are plotted for a crack depth of $a/d = 11.25\%$. Here again the vibrational behaviour of the experimental rotor can be approximated very well by the numerical simulation.

The following diagrams give some more results of the numerical simulation. In Fig. 22 the first three harmonics $\hat{v}_{k\Omega}$ of node 6 for a rotor speed of $n = 1560$ rpm and $n = 3060$ rpm are plotted against the related crack depth a/d in the range from 0% to 10% where the first beach mark could be set in the experiments. The increase of the second harmonic is the largest and gives at first an indication for the existence of a crack. But the vibrational sensitivity of the rotor due to a small crack is very poor so that it is very difficult to detect cracks with a depth of $a/d \leqq 5\%$. This confirms the experimental experiences. Taking into account experimental results (compare Fig. 10) it can be said that the increase of the second harmonic with growing crack depth is larger at higher rotor speed, which is obvious from experiments as well as from numerical simulations.

5 Summary

The application of an advanced vibration monitoring technique in laboratory tests shows that cracks of a depth of at least 5% of the rotor diameter are detectable. The results of calculations of a spatial finite element of the cracked rotor region are used for the derivation of a crack element of beam type. Together with other elements it is possible to carry out numerical simulations of the vibrational behaviour of the cracked experimental rotors. The results of the numerical simulations are in good agreement with measurements and may thus be a suitable tool in case, when experiments cannot be performed.

Acknowledgement

This work has been supported by the 'Deutsche Forschungsgemeinschaft' under contract numbers Po 136/11-1 and Po 136/11-2 which is highly appreciated.

References

1. Allianz Berichte: Schwingungsüberwachung von Turbosätzen – ein Weg zur Erkennung von Wellenanrissen. Berlin, München: Allianz-Berichte für Betriebstechnik und Schadensverhütung Nr. 24, 1987
2. Andersson, I.; Ericson, U.; Noremark, A.: Experience from on-line computerized vibration monitoring in scandinavian nuclear power plants during 1980–1986. In: Proc. of the 3rd EPRI Incipient-Failure Detection Conference, Philadelphia, Pennsylvania, Mar. 10–12, 1987, pp. 2-87–2-116, Report CS-5395, 1988
3. Chaudhary, A. B.; Bathe, K.-J.: A solution method for static and dynamic analysis of three-dimensional contact problems with friction. Comp. Struct. 24 (1986) 855–873

4. Dirr, B. O.; Schmalhorst, B. K.: Crack depth analysis of a rotating shaft by vibration measurement. Trans. ASME Journal of Vibration, Stress and Reliability in Design 110 (1988) 158–164
5. Höxtermann, E.: Erfahrungen mit Schäden in Form von Anrissen und Brüchen an Dampfturbinenwellen, Radscheiben und Generatorläufern. VGB Technische Vereinigung der Großkraftwerksbetreiber E.V., VGB Technisch-wissenschaftliche Berichte Wärmekraftwerke-VGB-TW 107-, 1988
6. Imam, I.: Method for on-line detection of incipient cracks in turbine-generator rotors. United States Patent No. 4,408,294, 1983
7. Imam, I.; Scheibel, J.; Azzaro, S. H.; Bankert, R. J.: Development of an on-line rotor crack detection and monitoring system. In: ASME (ed.) Proc. of the 11th Biennial Conference on Mechanical Vibation and Noise, Boston, 1987 – Rotating Machinery Dynamics DE-Vol. 2, pp. 615–628, 1987
8. Jenkins, L. S.: Cracked shaft detection on large vertical nuclear reactor coolant pump. In: Instability in Rotating Machinery – NASA Conf. Publication 2409, pp. 253–266, 1985
9. Kottke, J. J.; Menning, R. H.: Detection of a transverse crack in a turbine shaft – 'The Oak Creek Experience'. ASME Paper 81-JPGC-Pwr-19, 1981
10. Nilsson, L. R. K.: On the vibration behaviour of a cracked rotor. In: IFToMM (ed.) Proc. Int. Conf. on Rotordynamic Problems in Power Plants, Rome, 1982, pp. 507–514
11. Rothkegel, W.: Detection of small cracks in rotating shafts by vibration monitoring. Machine Vibration **1** (1992) 80–85
12. Rothkegel, W.: Rißerkennung bei Rotoren durch Schwingungsüberwachung. Hannover, Universität, Fakultät für Maschinenwesen, Diss. 1992. – Fortschr.-Ber. VDI Reihe 11, Nr. 180. Düsseldorf: VDI-Verlag 1993
13. Schmalhorst, B.: Experimentelle und theoretische Untersuchungen zum Schwingungsverhalten angerissener Rotoren. Hannover, Universität, Fakultät für Maschinenwesen, Diss. 1989. – Fortschr.-Ber. VDI Reihe 11, Nr. 117. Düsseldorf: VDI-Verlag 1989

Received May 3, 1993

Dr.-Ing. B. O. Dirr,
Prof. Dr.-Ing. K. Popp,
Dr.-Ing. W. Rothkegel
Universität Hannover,
Institut für Mechanik,
Appelstr. 11,
D-30167 Hannover
Germany